

A robust mechanical sensorless control strategy for active rectification of small wind turbines

Adrien Prévost, Vincent Léchappé, Romain Delpoux, Xavier Brun

Abstract—This article proposes a mechanical sensorless control strategy for the synchronous rectification of small wind turbines equipped with a surface-mounted Permanent Magnet Synchronous Generator (PMSG). By means of Lyapunov theory, the Globally Asymptotically Stable (GAS) of the closed loop system is proven. It allows the use of a classical Sliding Mode Observer (SMO) to remove the mechanical sensor in the control loop despite uncertainties on the resistance and inductance parameters. The analysis of the equilibrium points have made it possible to propose an analytic model of the angular misalignment between the true and the observer rotating frames, responsible for current tracking errors. Experimental tests on a wind turbine emulator show that despite large errors on the the resistance and inductance parameters, the impact on the energy harvest is low, proving that the strategy’s performance is robust to high uncertainties.

Index Terms—Wind Energy Conversion System (WECS), PMSG, robustness, mechanical sensorless control, sliding mode observer, synchronous rectifier

I. INTRODUCTION

SYNCHRONOUS rectification can increase energy production of PMSG based small wind turbines in comparison with the most widespread diode rectifier solution [1], [2]. This energy conversion strategy requires the knowledge of the rotor electrical angular position to apply Field Oriented Control (FOC). It is classically obtained with a position sensor which can be source of failures and adds extra design costs. Position sensorless FOC allows the implementation of fully mechanical sensorless wind turbine control laws (i.e. without position nor anemometer sensor), a domain of high interest in the literature [3]–[6]. A Back Electromotive Force (BEMF) observer is typically employed to reconstruct the electrical angle and velocity. This type of observer is model-based and requires the knowledge of the electrical parameters, namely Permanent Magnet (PM) flux linkage, inductance and resistance. In the area of small wind turbines, these parameters are not always well known and may vary for each wind turbine site. The generator manufacturing process can also be source of parameter uncertainty, in particular when the machines are hand-crafted [7]. Moreover, some elements are specific, such as the length and section of the transmission cable. It implies that for an identical generator, there could be different set of parameters. Finally, some parameters can also vary during operation. Typically, the winding resistance and flux linkage

are affected by the operating temperature and the inductance can saturate.

The use of model-based observers with wrong electrical parameters unavoidably leads to angle estimation errors [8]–[11] which has given rise to several works. For instance in [8], angle observation errors due to wrong inductance and resistance parameters were quantified for a BEMF linear extended observer. In [12], a method to reduce the observation error due to inductance saturation was proposed based on the concept of artificial inductance. In [13], an effective position error compensation method based on a disturbance observer is employed and shows very good results for variations of inductance. These methods address the problem of parameters variation during operation and requires a good knowledge of the q-axis inductance, but they are not suited for the parameter uncertainty issue. In [14], five amongst the most promising BEMF observers for surface mounted synchronous PM machines including a robust adaptive algorithm were compared experimentally. Tests with a 50% error on the inductance value resulted in significant position estimation errors for all observers. Another strategy rely on parameter identification. It can be performed online [15] and without mechanical sensor [16]. To obtain the real system parameters, the identification should be conducted in situ, without position sensor and embedded in the final hardware (e.g. microcontroller), which adds extra software complexity. Moreover, some identification methods require specific experimental setups which are not compatible with wind turbine application (e.g. shaft speed being imposed by another motor [17]).

Finally, even if a parameter identification method is embedded in the wind turbine system, obtaining the exact machine parameters over the whole speed and temperature ranges remains a challenge. For the reasons mentioned above, the ideal case where the system parameters are perfectly known is unrealistic.

The goal of this article is to propose a robust mechanical sensorless strategy for small wind turbines with a non-salient PMSG which electrical parameters are highly uncertain. In this scope, our first contribution is the finding of a controller gain condition implying that the system is GAS. Based on an existing Sliding Mode Observer (SMO), the second contribution consists in proposing gain tuning conditions of the observer to ensure its stability despite uncertainties on the resistance and inductance. The third contribution is the derivation of an analytical model to compute the influence of parameter errors on the generator operating points. Although studied in the case of an Axial Flux Permanent Magnet (AFPM) generator, the presented results are valid for all Surface mounted Permanent

Adrien Prévost, Vincent Léchappé, Romain Delpoux and Xavier Brun are with Univ Lyon, INSA Lyon, Université Claude Bernard Lyon 1, Ecole Centrale de Lyon, CNRS, Ampère, UMR5005, 69621 Villeurbanne, France (e-mail: adrien.prevost@insa-lyon.fr; vincent.lechappe@insa-lyon.fr; romain.delpoux@insa-lyon.fr; xavier.brun@insa-lyon.fr)

Magnet Synchronous Machines. Finally, in terms of energy harvesting, it is shown experimentally that the performance of the sensorless strategy is robust to large parameter uncertainties. The paper is organized as follows. The WECS is modelled in Section II. The WECS control scheme is described in Section III and the observer is designed in Section V. The robustness analysis of the closed-loop system is conducted in Section VI. In Section VII, the effectiveness of the proposed strategy is demonstrated experimentally and discussed.

II. MODELLING OF THE WECS

A schematic of the WECS architecture is given on Fig. 1.

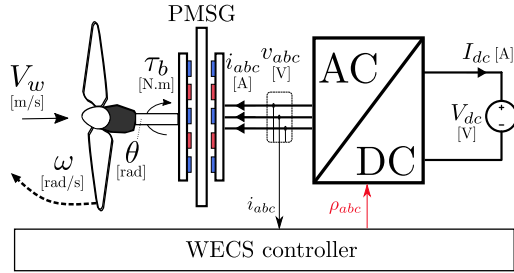


Fig. 1. The Wind Energy Conversion System (WECS) architecture.

A. Aerodynamics

The aerodynamic efficiency of the wind turbine rotor is commonly modelled with the power coefficient C_p which enables to write an expression of the aerodynamic power extracted from the wind by the blades

$$P = \frac{1}{2} \rho_{air} A V_w^3 C_p(\lambda), \quad (1)$$

with A the rotor swept area, ρ_{air} the air density and V_w the wind velocity.

The case-study wind turbine blades have a fixed pitch, thus C_p varies in function of the Tip Speed Ratio (TSR) λ written as

$$\lambda = \frac{\omega \cdot R_r}{V_w} \quad (2)$$

where ω is the rotor angular velocity and R_r the rotor radius. By conservation of power, the aerodynamic torque applied by the blades on the shaft can be written as

$$\tau_b = \frac{P}{\omega}. \quad (3)$$

B. Rotating system

The wind turbine is direct-drive, hence the rotor dynamics can be expressed as a single inertia equivalent system given by

$$J \frac{d\omega}{dt} = \tau_b + \tau_g - b\omega \quad (4)$$

with τ_g the electromagnetic torque applied by the PMSG, J and b the total rotating system inertia and damping coefficient respectively.

C. Generator

Here, we consider a non-salient PMSG. The corresponding current dynamics in motor convention are given by

$$L \frac{di_{abc}}{dt} = v_{abc} - Ri_{abc} - e_{abc} \quad (5)$$

with R the phase resistance, L the phase inductance, $v_{abc} = [v_a \ v_b \ v_c]^T$ the phases voltages, $i_{abc} = [i_a \ i_b \ i_c]^T$ the phase currents and $e_{abc} = [e_a \ e_b \ e_c]^T$ the BEMFs. The latter are induced by the PMs according to

$$e_{abc} = \frac{d}{dt} \lambda_r. \quad (6)$$

The PM flux linkage component λ_r is given by

$$\lambda_r = \phi_f \begin{bmatrix} \cos(\theta_e) \\ \cos(\theta_e - \frac{2\pi}{3}) \\ \cos(\theta_e + \frac{2\pi}{3}) \end{bmatrix} \quad (7)$$

with ϕ_f the peak magnetic flux of the PMs seen by a stator phase winding and θ_e the rotor angular electrical position.

Through Clarke transformation, it is possible to write the generator currents' dynamics in the $\alpha - \beta$ frame such as

$$\frac{di_{\alpha\beta}}{dt} = \frac{1}{L} v_{\alpha\beta} - \frac{R}{L} i_{\alpha\beta} - \frac{1}{L} e_{\alpha\beta}, \quad (8)$$

with the BEMF in the $\alpha - \beta$ frame given by

$$e_{\alpha\beta} = p\phi_f\omega \begin{bmatrix} -\sin(\theta_e) \\ \cos(\theta_e) \end{bmatrix}. \quad (9)$$

Park transformation allows describing the machine behavior in the $d - q$ rotating frame which is conveniently used for FOC. Its construction usually requires the knowledge of the rotor angular electrical position since it is defined as

$$\mathcal{P}(\theta_e) = \begin{bmatrix} \cos(\theta_e) & \sin(\theta_e) \\ -\sin(\theta_e) & \cos(\theta_e) \end{bmatrix} \quad (10)$$

with $x_{dq} = \mathcal{P}(\theta_e)x_{\alpha\beta}$ expressing the projection of the variable x from $\alpha - \beta$ to $d - q$ frame. In the case of a non-salient PMSG, the currents' dynamics in the $d - q$ frame are given by

$$L \frac{di_{dq}}{dt} = v_{dq} - Ri_{dq} - p\omega L \begin{bmatrix} 0 & -1 \\ 1 & 0 \end{bmatrix} i_{dq} - p\phi_f\omega \begin{bmatrix} 0 \\ 1 \end{bmatrix} \quad (11)$$

with p the pole pairs number. The electromagnetic torque of the PMSG is proportional to the quadrature axis current according to

$$\tau_g = \frac{3}{2} p\phi_f i_{dq}. \quad (12)$$

Remark 1. The rectifier used in the article a classical three legs with two levels voltage source converter structure. The electrical power at the rectifier output is given by $P_{dc} = V_{dc} \cdot I_{dc}$.

III. WECS CONTROL SCHEME

A. Problem statement

Let R_o , L_o be the assumed parameters values used to design the WECS control law such as

$$R_o = R + \delta_R, \quad L_o = L + \delta_L \quad (13)$$

with the closed-loop equilibrium states in the d and q axis given by

$$\begin{cases} x_{i_d^*} &= \frac{-(k_p + R)i_d^\# + pL\omega^*i_q^\#}{k_i}, \\ x_{i_q^*} &= \frac{-(k_p + R)i_q^\# - pL\omega^*i_d^\# - p\phi_f\omega^*}{k_i}. \end{cases} \quad (23)$$

Given these definitions, eqs. (20) and (21) can be re-written as

$$\begin{cases} v_d &= -k_p(e_d + i_d^\#) - k_i(e_{id} + x_{i_d^*}), \\ \dot{x}_{id} &= e_d \end{cases} \quad (24)$$

for the d axis, and

$$\begin{cases} v_q &= -k_p(e_q + i_q^\#) - k_i(e_{iq} + x_{i_q^*}) \\ \dot{x}_{iq} &= e_q \end{cases} \quad (25)$$

for the q axis.

Hence the closed loop system dynamics can be given by

$$\begin{cases} \dot{e}_d &= \frac{-(k_p + R)e_d - k_i e_{id}}{L} \\ &+ p(e_\omega + \omega^*)e_q + p e_\omega i_q^\# \\ \dot{e}_q &= \frac{-(k_p + R)e_q - k_i e_{iq} - p\phi_f e_\omega}{L} \\ &- p(e_\omega + \omega^*)e_d - p e_\omega i_d^\# \\ \dot{e}_{id} &= e_d \\ \dot{e}_{iq} &= e_q \\ \dot{e}_\omega &= \frac{3}{2} \frac{p\phi_f}{J} e_q - \frac{b}{J} e_\omega \end{cases} \quad (26)$$

Theorem 1. *The closed-loop system given by eq. (26) is GAS if the following condition is met*

$$\begin{cases} k_p &> a - R \\ k_i &> 0 \end{cases} \quad (27)$$

$$\text{with } a = \frac{3}{4b} p\phi_f \sqrt{p^2(\phi_f + Li_d^\#)^2 + (Li_q^\# p)^2} - \frac{3p^2\phi_f(\phi_f + Li_d^\#)}{4b}.$$

The proof is detailed in the Appendix.

Remark 3. *In Ortega et al. [19], a similar result is given for a classical PI controller structure and a current reference in the d axis set to zero ($i_d^\# = 0$). Our result is different and complementary since the controller is a state feedback with integral action and the reference $i_d^\#$ does not need to be zero.*

If $i_d^\# = 0$, as in eq. (17), the expression of a can be simplified

$$a = -\frac{3p\phi_f \left(p\phi_f - \sqrt{p^2(L^2 i_q^{\#2} + \phi_f^2)} \right)}{4b} \quad (28)$$

From eqs. (27) and (28), the minimum value of the gain k_p to guarantee the system stability can be computed according to the system parameters (ϕ_f, p, R, L, b) and the current set-point $i_q^\#$. To ensure stability in the whole operating range, k_p should be calculated considering the maximum value of the current reference. One can deduce that the gain k_p is likely

to be high if the maximum current reference is high and the friction coefficient is low.

Remark 4. *In presence of uncertainties on the parameters R, L , the assumed values R_{min} and L_{max} shall be used to calculate k_p .*

Remark 5. *Theorem 1 does not cover the stability of the OTC law, which was already addressed by Johnson et al. [18].*

V. OBSERVER DESIGN

A. Currents observer design

The goal here is to design an observer which can lead to the reconstruction of the equivalent Park transformation \mathcal{P}_{e_q} in spite of uncertainties on the electrical parameters R and L .

Define the following current SMO [20, p. 266] as

$$\frac{d\hat{i}_{\alpha\beta}}{dt} = \frac{1}{L_o} v_{\alpha\beta} - \frac{R_o}{L_o} \hat{i}_{\alpha\beta} - \frac{l_1}{L_o} \text{sign}(\hat{i}_{\alpha\beta} - i_{\alpha\beta}) \quad (29)$$

where l_1 is the sliding mode gain. Subtraction of Eq. (8) to (29) gives rise to the sliding surface $s_{\alpha\beta} = \hat{i}_{\alpha\beta} - i_{\alpha\beta}$ which mismatch dynamics are given by

$$\frac{ds_{\alpha\beta}}{dt} = \frac{1}{L} e_{\alpha\beta} + \frac{1}{L_o} \Pi_{\alpha\beta} - \frac{R_o}{L_o} s_{\alpha\beta} - \frac{l_1}{L_o} \text{sign}(s_{\alpha\beta}). \quad (30)$$

Here, the term $\Pi_{\alpha\beta}$ contains the perturbations due to parameter uncertainties according to

$$\Pi_{\alpha\beta} = \frac{R\delta_L - \delta_R L}{L} i_{\alpha\beta} - \frac{\delta_L}{L} v_{\alpha\beta}. \quad (31)$$

When the parameters are perfectly known meaning that $\delta_L = 0$ and $\delta_R = 0$, the term $\Pi_{\alpha\beta}$ is equal to zero. In this academic case, the condition on the gain $l_1 > \max(|e_\alpha|, |e_\beta|)$ implies that $s_{\alpha\beta} \dot{s}_{\alpha\beta} < 0$, leading to sliding mode after a finite time interval. However, in the presence of uncertainties on L and R , this condition should be revised. Indeed, when $\Pi_{\alpha\beta} \neq 0$ the condition $s_{\alpha\beta} \dot{s}_{\alpha\beta} < 0$ necessary to sliding mode implies that

$$l_1 > \max \left(\left| \frac{L_o}{L} e_\alpha + \Pi_\alpha \right|, \left| \frac{L_o}{L} e_\beta + \Pi_\beta \right| \right). \quad (32)$$

In practice, condition described by Eq. (32) is not straight forward to use as is. Hence, we propose another condition on l_1 which is function of the parameters bounds and system extreme operating points. Let us define the maximum $\alpha - \beta$ frame axis BEMF, phase voltage and current amplitudes E_{max} , V_{max} and I_{max} such as

$$\begin{aligned} E_{max} &= \max(|e_\alpha|, |e_\beta|), \\ V_{max} &= \max(|v_\alpha|, |v_\beta|), \\ I_{max} &= \max(|i_\alpha|, |i_\beta|). \end{aligned} \quad (33)$$

The following condition guarantees that $s_{\alpha\beta} \dot{s}_{\alpha\beta} < 0$ provided that Assumption 1 holds (see proof in Appendix)

$$l_1 > \frac{L_o}{L_{min}} E_{max} + \left(R_{max} \frac{\Delta_L}{L_{min}} + \Delta_R \right) I_{max} + \frac{\Delta_L}{L_{min}} V_{max} \quad (34)$$

with $\Delta_R = R_{max} - R_{min} > 0$ and $\Delta_L = L_{max} - L_{min} > 0$.

The computation of l_1 requires a knowledge of the extreme operating points E_{max} , V_{max} and I_{max} of the system. However, this necessitates to find the equilibrium points of the closed loop system in presence of parameter uncertainties. This could be achieved by modelling the BEMF observation error due to these uncertainties. The next subsection will detail the BEMF observer. Following this, a modelling of the observation error will be proposed in Section VI.

B. BEMF and speed observer

Assume that l_1 is chosen so that the condition $s_{\alpha\beta}\dot{s}_{\alpha\beta} < 0$ is satisfied, then sliding mode occurs after a finite time interval. Once the sliding surface is reached, $s_{\alpha\beta} = \dot{s}_{\alpha\beta} = 0$ which results in the chattered signal

$$z_{\alpha\beta} = l_1 \text{sign}(\bar{s}_{\alpha\beta}) = \frac{L_o}{L} e_{\alpha\beta} + \Pi_{\alpha\beta} + \Pi_{HF} \quad (35)$$

with Π_{HF} the perturbation due to the high frequency switching action. To obtain the smooth estimates $\hat{e}_{\alpha\beta}$, the $z_{\alpha\beta}$ signals needs to be low-pass filtered. The observer detailed in [20, p. 267] has low-pass filtering properties and the advantage of providing an estimate $\hat{\omega}$ of the rotational velocity. We propose a slightly modified version of this observer by inserting the gain l_3 such as

$$\begin{cases} \frac{d\hat{e}_\alpha}{dt} = -\hat{\omega}_e \hat{e}_\beta - l_2(\hat{e}_\alpha - z_\alpha), \\ \frac{d\hat{e}_\beta}{dt} = \hat{\omega}_e \hat{e}_\alpha - l_2(\hat{e}_\beta - z_\beta), \\ \frac{d\hat{\omega}_e}{dt} = l_3 [(\hat{e}_\alpha - z_\alpha)\hat{e}_\beta - (\hat{e}_\beta - z_\beta)\hat{e}_\alpha], \end{cases} \quad (36)$$

where $\omega_e = p\omega$ is the electrical rotational velocity and $l_2 > 0$, $l_3 > 0$ are constant observer gains. The convergence of the observer is proven for $l_2 > 0$, $l_3 = 1$ and without parameter uncertainty [20, p. 267]. Choosing $l_3 > 1$ has shown to accelerate the convergence of $\hat{\omega}_e$ to ω_e . The convergence proof for the general case is out of the scope of this article.

VI. ROBUSTNESS ANALYSIS

A. Modelling of the BEMF observation error

Thanks to the low-pass filter property of Eq. (36), the high frequency Π_{HF} are filtered, and one obtains

$$\hat{e}_{\alpha\beta} = \frac{L_o}{L} e_{\alpha\beta} + \frac{R\delta_L - \delta_R L}{L} \mathcal{P}^{-1}(\theta_e) i_{dq} - \frac{\delta_L}{L} \mathcal{P}^{-1}(\theta_e) v_{dq} \quad (37)$$

at the observer output. Rewriting (11) at steady state gives the expression of v_{dq} at equilibrium given by

$$v_{dq}^* = R i_{dq}^* + p\omega L \mathcal{J} i_{dq}^* + e_{dq}^*. \quad (38)$$

Substituting Eqs. (9) and (38) in Eq. (37) enables to write an expression of the BEMFs estimates at equilibrium

$$\begin{cases} \hat{e}_\alpha = -x \sin(\theta_e) + y \cos(\theta_e), \\ \hat{e}_\beta = x \cos(\theta_e) + y \sin(\theta_e), \\ x = p\omega(\phi_f - i_d^* \cdot \delta_L) - \delta_R \cdot i_q^*, \\ y = -i_d^* \cdot \delta_R + i_q^* \cdot p\omega \delta_L. \end{cases} \quad (39)$$

The steps leading to Eq. (39) are detailed in Appendix. From trigonometric identities, one can write

$$\hat{e}_{\alpha\beta} = \sqrt{x^2 + y^2} \begin{bmatrix} -\sin(\theta_e + \varphi) \\ \cos(\theta_e + \varphi) \end{bmatrix} \quad (40)$$

with the angle φ given at steady state by

$$\varphi^*(i_{dq}, \delta_R, \delta_L, \omega) = \begin{cases} -\arctan\left(\frac{y}{x}\right) & \text{if } x > 0 \\ -\arctan\left(\frac{y}{x}\right) + \pi & \text{otherwise} \end{cases} \quad (41)$$

Reminding Eq. (9), the angle φ appears to be the phase lag between $\hat{e}_{\alpha\beta}$ and $e_{\alpha\beta}$.

Eqs. (39) to (41) give an analytic description of the BEMF observation error in function of the uncertainties δ_R , δ_L on the parameters R and L . According to the model, the estimated BEMFs are delayed by a phase angle φ and also have a biased amplitude. As mentioned previously, the amplitude bias will not alter the Park transformation. As for the phase lag, it will bias the Park transformation, leading to a modified rotating frame $\hat{d} - \hat{q}$. From Eqs. (39), the phase lag φ between the original $d - q$ frame and the observer $\hat{d} - \hat{q}$ frame is not constant since it depends on the machine currents i_{dq} and the rotational velocity ω . This phenomenon is analog to a misaligned encoder [21], which misalignment would be dynamically depending on the machine operating points and the parameter uncertainties.

Since the currents controller will operate within the biased $\hat{d} - \hat{q}$ frame, an error will be introduced in the control of the currents i_{dq} . Hence, extra analysis is needed to determine on which true i_{dq} currents the system will stabilize.

B. A model of the currents equilibrium

In this section, the goal is to develop a simple analytical model of the equilibrium adopted by the true i_{dq} currents, given that their projections \hat{i}_{dq} are controlled within the biased $\hat{d} - \hat{q}$ frame. Let us write the projection of \hat{i}_{dq} in the $d - q$ frame

$$\begin{cases} i_d = \hat{i}_d \cos(\varphi) - \hat{i}_q \sin(\varphi), \\ i_q = \hat{i}_d \sin(\varphi) + \hat{i}_q \cos(\varphi). \end{cases} \quad (42)$$

From Eq. (42), it is possible to show that

$$i_d^2 + i_q^2 = \hat{i}_d^2 + \hat{i}_q^2, \quad (43)$$

which means that the amplitude of the current vector is conserved from one frame to the other. From Eqs. (41) and (39), it could be noticed that the resolution of Eq. (42) with respect to i_{dq} is not trivial. Hence, the following reasonable assumptions will be made.

Assumption 3. *The rotational velocity ω is positive.*

The case where ω is very small or null is not considered since this would result in the system being non-observable, removing the purpose of the analysis.

Assumption 4. *High torque values take place for high velocities.*

This assumption holds since through OTC, the currents follow the trajectory described by Eq. (17).

Assumption 5. The parameter uncertainties δ_L and δ_R are of the same order of magnitude that the parameters L and R .

Given eq. (17) and Assumption 5, one can write that $\phi_f \gg i_d \cdot \delta_L$, unless uncommon PMSG design where the PM flux would be very weak. This condition is verified for the PMSG parameters provided in Table II since $\phi_f \simeq 10^{-1}$ Wb and $L \simeq 10^{-3}$ H. Hence, let us write an approximation of x as

$$x' = p\phi_f\omega - \delta_R \cdot i_q^* \simeq x. \quad (44)$$

Assumptions 4 and 5 allow to write the inequality

$$p\phi_f\omega > \delta_R \cdot i_q^*, \quad (45)$$

meaning that the term a' of Eq. (44) is positive. Given the same assumptions, the term b should stay very small compared to x' leading to

$$x' \gg y. \quad (46)$$

From this, one can assume that the phase lag φ is small. Consequently, the trigonometric functions could be reasonably approximated by the first term of their Taylor expansion. Hence, the phase lag φ could be given by

$$\varphi = -\arctan\left(\frac{y}{x}\right) \simeq -\frac{y}{x'}, \quad (47)$$

and its projections in the trigonometric frame can be given by

$$\begin{aligned} \sin(\varphi) &\simeq -\frac{y}{x'}, \\ \cos(\varphi) &\simeq 1. \end{aligned} \quad (48)$$

By injecting Eq. (48) in (42), the problem can be written at equilibrium such as

$$\begin{aligned} i_d^* &\simeq \hat{i}_q^* \cdot \frac{y}{x'}, \\ i_q^* &\simeq \hat{i}_q^*. \end{aligned} \quad (49)$$

At equilibrium, the resolution of Eq. (49) leads to a simple expression of i_d

$$i_d^* \simeq \frac{\delta_L i_q^{\#2}}{\phi_f}. \quad (50)$$

From Eq. (49) one can write that $\text{sign}(i_q) = \text{sign}(i_q^{\#})$. Bearing in mind that the norm of the current is not changing from $d-q$ to $\hat{d}-\hat{q}$ frame, a more accurate approximation of i_q can be found by injecting the approximation of i_d found above in Eq. (43), which leads to

$$i_q^* \simeq \text{sign}(i_q^{\#}) \cdot \sqrt{\frac{\phi_f \sqrt{4\delta_L^2 i_q^{\#2} + \phi_f^2} - \phi_f^2}{2\delta_L^2}} \quad (51)$$

Hence, Eqs. (50) and (51) give an analytical model of the true i_{dq} currents equilibrium in function of the uncertainty on the parameters and the $i_q^{\#}$ current reference. It is interesting to note that according to the model, the parametric uncertainty δ_R does not introduce any error on i_{dq} . Hence, this model can be used to quantify the deviation of the system from the desired operating points in function of the parametric uncertainty δ_L . Of course, using Eq. (51) with $\delta_L = 0$ is of no interest.

VII. RESULTS AND DISCUSSION

Experiments were conducted on the wind turbine emulator [22] shown on Fig. 3. The latter is made of a PMSG and a Permanent Magnet Synchronous Motor (PMSM) connected by their shaft through a torque meter. The PMSM is controlled so that the torque of the turbine blades is emulated. A first

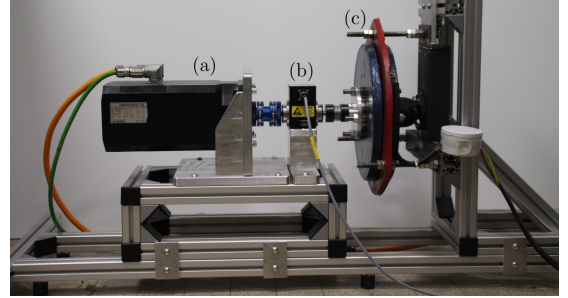


Fig. 3. Wind turbine emulator test bench. (a) PMSM (b) Torque-meter (c) axial flux PMSG

experiment was conducted under turbulent wind conditions, reported on Fig. 4, generated with TurbSim software using a Kaimal spectrum and an average wind velocity of 6 m/s. Tests were conducted with the same wind data first with an encoder and with the observer. For each of these tests, different values of the parameters L_o , R_o were provided. A second experiment was conducted with stationary wind conditions. This allows to measure the impact of parameter uncertainties on the power output over the whole wind speed range [0–10] m/s of the "zone 2" operating zone. All the parameters used in the experimental setup are summarized in Table II. The aerodynamic coefficient $C_p(\lambda)$ is issue from [23].

A. Tracking performance

1) *Currents:* The currents tracking errors $\epsilon_{dq} = e_{dq} = i_{dq}^{\#} - i_{dq}$ are plotted on Figs. 5 and 6 respectively for each parameter uncertainties scenario. It can be seen that the

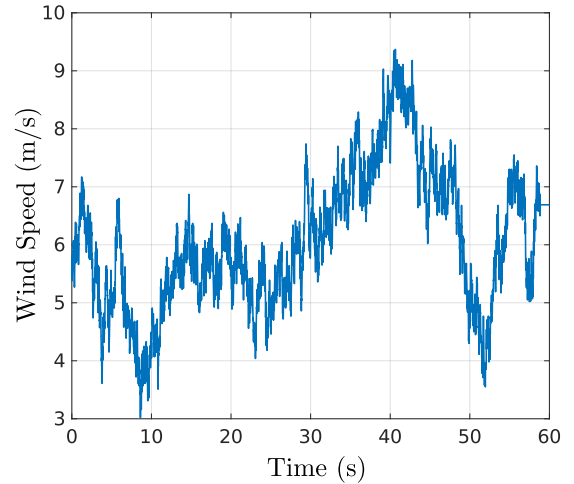


Fig. 4. The turbulent wind velocity time series

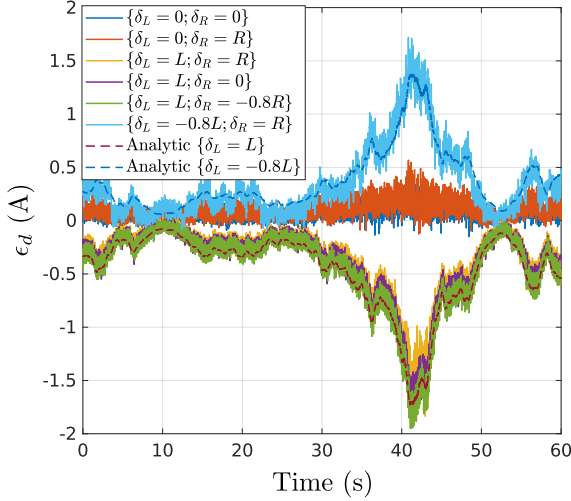


Fig. 5. Tracking error of the current i_d for different scenario of parameters uncertainty. Experimental data are plotted in continuous lines and results from the analytical model in dashed.

tracking error is close to zero when the correct inductance value is provided to the observer (i.e. $\delta_L = 0$). However, when $\delta_L \neq 0$, it can be observed that a tracking error is introduced. The analytical tracking errors from Eqs. (50) and (51) are plotted in dashed lines for the scenario $\delta_L = -0.8L$ and $\delta_L = L$. On Fig. 5, one can see that the tracking error amplitude ϵ_d rises when the wind velocity increases. Indeed, as wind velocity rises, the aerodynamic torque increases, leading to a surge of the rotor speed which, through OTC (Eq. (17)) raises the current setpoint $i_q^\#$ amplitude. According to Eq. (50), this causes an increase of the i_d current amplitude, despite the fact that $i_d^\# = 0$. It is interesting to note that a non-desired flux weakening occurs in the cases where $\delta_L < 0$, which is coherent with the analytical model. It can be seen that the evolution of ϵ_d computed with the model fits well with the experimental data in average value. Despite up to 2A of negative current on the direct current i_d , the overall energy harvest, shown Fig. 10, was not impacted significantly. Indeed, the currents' norm $\|i_{dq}\|$ as mentioned in (43), remains unchanged. It leads to no extra joule loss but a slight torque production reduction, see Eq. (51), which does not affect the aerodynamic operating point of the generator, see Fig. 8. The tracking error ϵ_q represented on Fig. 6 is also close to zero when the uncertainty on the inductance is zero, which means that the reference torque computed by OTC is correctly tracked. In the cases where $\delta_L \neq 0$, negative tracking errors were recorded which amplitudes also increase with wind speed for the reasons explained above. This is also well-fitted in average by the curves computed from the analytical model described by Eq. (51). This negative tracking error on i_q results in a part of the torque being lost in reactive power.

2) *Rotational velocity*: The speed tracking error $\bar{\omega} = \hat{\omega} - \omega$ is represented on Fig. 7. It stays close to zero for all uncertainties scenarios, which is crucial since the rotational velocity is used by OTC to compute the currents references.

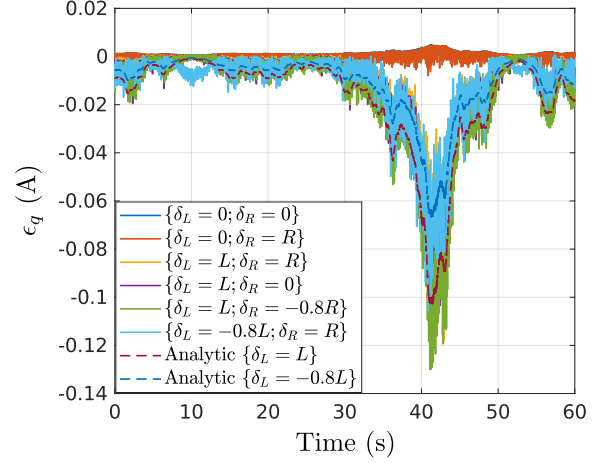


Fig. 6. Tracking error of the current i_q for different scenario of parameter uncertainties. Experimental data are plotted in continuous lines and results from the analytical model in dashed.

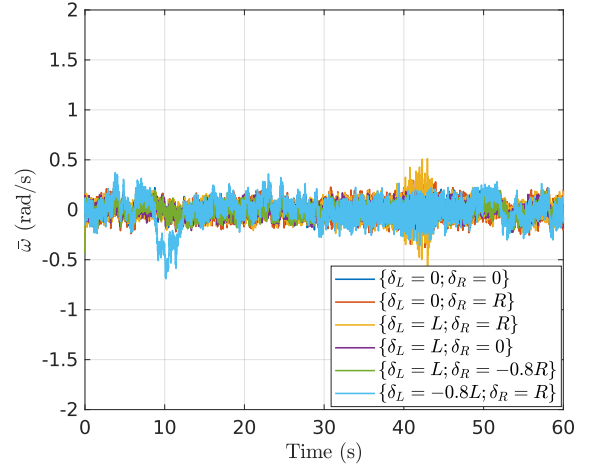


Fig. 7. Speed observation error for several scenario of parameters uncertainty in turbulent wind conditions.

3) *Tip Speed Ratio*: The TSR is plotted on Fig. 8. It can be seen that parameter uncertainties have no impact on it since it stays close to the optimal TSR $\lambda_{opt} = 5.75$. It shows that OTC is not affected by the parameter uncertainties. Indeed, since the tracking errors on the currents and the rotational velocity are small, the impact on the generator torque is not significant. This results in identical aerodynamic behaviors.

B. Energy harvesting

It can be seen on Fig. 9 that for dynamic conditions, the uncertainty on parameters does not affect the output power. This result is not surprising since the tracking error on i_q was shown to remain small in spite of high uncertainty on the parameters, which leads to close aerodynamic operating points as seen with the TSR on Fig. 8. It should be reminded that only currents references are used to control the generator and that the norm of the currents are the same in both $d-q$

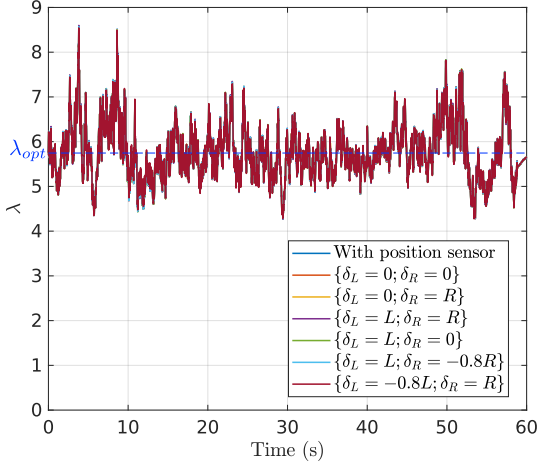


Fig. 8. Effect of the uncertainties on the TSR for turbulent wind.

and $\hat{d} - \hat{q}$ frames. Hence, an angle observation error shall not introduce additional joules losses in comparison to the encoder scenario. Let us define the optimal energy harvest as

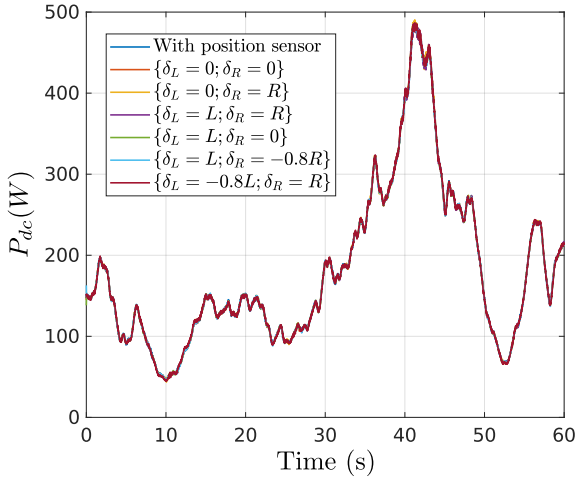


Fig. 9. Power at the rectifier output for several system configurations and scenario of parameters uncertainty.

$$W_{opt} = \int_0^T \frac{1}{2} \rho_{air} A V_w(t)^3 C_{p(max)} dt \quad (52)$$

with T the duration of the wind velocity time series. This energy corresponds to an ideal scenario where the aerodynamic efficiency would stay always optimal (i.e. $C_p = C_{p(max)}$) while the generator-rectifier efficiency would be unity. The energetic efficiency η_E over the period T is given by

$$\eta_E = \frac{\int_0^T P_{dc}(t) dt}{W_{opt}} = \frac{W}{W_{opt}}. \quad (53)$$

The energy harvest W for each system configuration and parameter uncertainties scenario together with the optimal energy harvest W_{opt} are plotted on Fig. 10. A summary of the energy yield is shown on Table I. The control strategy allowed

to harvest 80% of available energy W_{opt} despite parameter uncertainties.

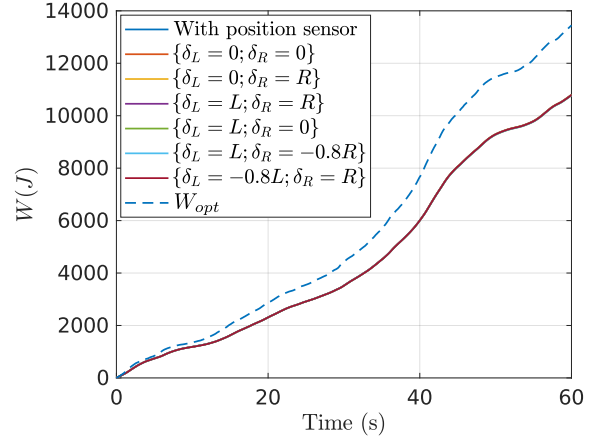


Fig. 10. WECS energy yield.

Configuration	δ_L	δ_R	AEP (kWh)	η_E
Encoder	-	-	1183	0.80
Sensorless	0	0	1167	0.80
Sensorless	0	R	1167	0.80
Sensorless	L	R	1164	0.80
Sensorless	L	0	1166	0.80
Sensorless	L	-0.8R	1163	0.80
Sensorless	-0.8L	R	1162	0.80

TABLE I
PERFORMANCE'S SUMMARY OF THE CONTROL STRATEGY.

C. Annual Energy Production

The power curves measured during the experiments under stationary wind are represented on Fig. 11. The truncated Annual Energy Production (AEP) was computed [24] for a Rayleigh distribution with an average wind velocity of 5 m/s. Amongst the different scenario of parameter uncertainties, the AEP is at least 98% of the AEP obtained with an encoder.

VIII. CONCLUSION

In this work, a mechanical sensorless control strategy for small wind turbines with a surface mounted PMSG was designed and analyzed regarding parameter uncertainties. Under a constant or slowly varying blades torque, we proved that the system is GAS. Additionally, a condition was provided on the SMO gain to ensure convergence in spite of the uncertainties. The modelling of the steady state tracking error of the machine currents allowed to illustrate the robustness of the proposed approach. Experiments were conducted on a wind turbine emulator to investigate how the tracking errors would impact the behavior of the WECS. The analytical model gave a good approximation of the experimental average tracking errors when compared to experimental data. In both stationary and turbulent wind conditions, the sensorless strategy performance was similar to the configuration with an encoder, in spite of the

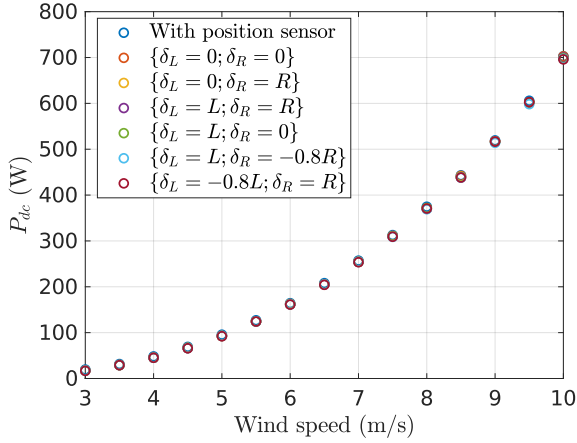


Fig. 11. Comparison of power curves of the WECS under for several scenario of parameter uncertainties.

uncertainties on the parameters. Hence, sensorless control of PMSGs does not necessarily degrade the power performance of WECSs under active rectification. Overall, the algorithm could be implemented on a standard synchronous rectifier controller with a 'generic' set of electrical parameters. In future works, it may be interesting to extend the control law to the zone III and investigate how parameter uncertainties affect its behavior in the stall region.

REFERENCES

- [1] A. Mirecki, X. Roboam, and F. Richardeau, "Architecture Complexity and Energy Efficiency of Small Wind Turbines," *IEEE Transactions on Industrial Electronics*, vol. 54, no. 1, pp. 660–670, Feb. 2007.
- [2] A. Prévost, R. Delpoux, V. Léchappé, K. Latoufis, and X. Brun, "Experimental Comparison of Passive and Synchronous Rectification on a Locally Manufactured Small Wind Turbine," in *2023 6th International Conference on Renewable Energy for Developing Countries (REDEC)*, pp. 84–89. Zouk Mosbeh, Lebanon: IEEE, Jul. 2023.
- [3] J. Brahmi, L. Krichen, and A. Ouali, "A comparative study between three sensorless control strategies for PMSG in wind energy conversion system," *Applied Energy*, vol. 86, no. 9, pp. 1565–1573, Sep. 2009.
- [4] W. Qiao, X. Yang, and X. Gong, "Wind Speed and Rotor Position Sensorless Control for Direct-Drive PMG Wind Turbines," *IEEE Transactions on Industry Applications*, vol. 48, no. 1, pp. 3–11, Jan. 2012.
- [5] G. Buticchi, E. Lorenzani, F. Immovilli, and C. Bianchini, "Active Rectifier With Integrated System Control for Microwind Power Systems," *IEEE Transactions on Sustainable Energy*, vol. 6, no. 1, pp. 60–69, Jan. 2015.
- [6] R. Aubrée, F. Auger, M. Macé, and L. Loron, "Design of an efficient small wind-energy conversion system with an adaptive sensorless MPPT strategy," *Renewable Energy*, vol. 86, pp. 280–291, Feb. 2016.
- [7] K. Latoufis, G. Messinis, P. Kotsampopoulos, and N. Hatzigiorgiou, "Axial Flux Permanent Magnet Generator Design for Low Cost Manufacturing of Small Wind Turbines," *Wind Engineering*, vol. 36, no. 4, pp. 411–431, Aug. 2012.
- [8] T. Batzel and K. Lee, "Electric Propulsion With the Sensorless Permanent Magnet Synchronous Motor: Model and Approach," *IEEE Transactions on Energy Conversion*, vol. 20, no. 4, pp. 818–825, Dec. 2005.
- [9] S. Bolognani, S. Calligaro, and R. Petrella, "Design Issues and Estimation Errors Analysis of Back-EMF-Based Position and Speed Observer for SPM Synchronous Motors," *IEEE Journal of Emerging and Selected Topics in Power Electronics*, vol. 2, no. 2, pp. 159–170, Jun. 2014.
- [10] M. Seilmeier and B. Piepenbreier, "Impact of iron losses and parameter errors on back-EMF based sensorless control of PMSM," in *IECON 2014 - 40th Annual Conference of the IEEE Industrial Electronics Society*, pp. 634–640. Dallas, TX, USA: IEEE, Oct. 2014.

- [11] G. Wang, M. Valla, and J. Solsona, "Position Sensorless Permanent Magnet Synchronous Machine Drives—A Review," *IEEE Transactions on Industrial Electronics*, vol. 67, no. 7, pp. 5830–5842, Jul. 2020.
- [12] K. Lu, X. Lei, and F. Blaabjerg, "Artificial Inductance Concept to Compensate Nonlinear Inductance Effects in the Back EMF-Based Sensorless Control Method for PMSM," *IEEE Transactions on Energy Conversion*, vol. 28, no. 3, pp. 593–600, Sep. 2013.
- [13] M. Zhao, G. Liu, Q. Chen, Z. Liu, X. Zhu, and C. H. T. Lee, "Effective Position Error Compensation in Sensorless Control Based on Unified Model of SPMSM and IPMSM," *IEEE Transactions on Industrial Informatics*, vol. 19, no. 5, pp. 6750–6761, May. 2023.
- [14] A. Benevieri, M. Marchesoni, M. Passalacqua, and L. Vaccaro, "Experimental Low-Speed Performance Evaluation and Comparison of Sensorless Passive Algorithms for SPMSM," *IEEE Transactions on Energy Conversion*, vol. 37, no. 1, pp. 654–664, Mar. 2022.
- [15] Z. Q. Zhu, D. Liang, and K. Liu, "Online Parameter Estimation for Permanent Magnet Synchronous Machines: An Overview," *IEEE Access*, vol. 9, pp. 59059–59084, 2021.
- [16] R. Delpoux, M. Bodson, and T. Floquet, "Parameter estimation of permanent magnet stepper motors without mechanical sensors," *Control Engineering Practice*, vol. 26, pp. 178–187, 2014, publisher: Elsevier.
- [17] E. Armando, R. I. Bojoi, P. Guglielmi, G. Pellegrino, and M. Pastorelli, "Experimental Identification of the Magnetic Model of Synchronous Machines," *IEEE Transactions on Industry Applications*, vol. 49, no. 5, pp. 2116–2125, Sep. 2013.
- [18] K. E. Johnson, "Control of variable-speed wind turbines: standard and adaptive techniques for maximizing energy capture," *IEEE Control Systems*, vol. 26, no. 3, pp. 70–81, 2006.
- [19] R. Ortega, N. Monshizadeh, P. Monshizadeh, D. Bazylev, and A. Pyrkin, "Permanent magnet synchronous motors are globally asymptotically stabilizable with PI current control," vol. 98, DOI 10.1016/j.automatica.2018.09.031, pp. 296–301. [Online]. Available: <https://linkinghub.elsevier.com/retrieve/pii/S0005109818304564>
- [20] V. Utkin, J. Guldner, and J. Shi, *Sliding Mode Control in Electro-Mechanical Systems*, 2nd ed. Boca Raton: CRC Press, 2009.
- [21] R. Delpoux, M. Bodson, and T. Floquet, "Joint Identification of Stepper Motor Parameters and of Initial Encoder Offset," in *16th IFAC Symposium on System Identification*, Brussels, Belgique, 2012.
- [22] A. Prévost, V. Léchappé, R. Delpoux, and X. Brun, "An Emulator for Static and Dynamic Performance Evaluation of Small Wind Turbines," in *2023 IEEE 32nd International Symposium on Industrial Electronics (ISIE)*, pp. 1–6. Helsinki, Finland: IEEE, Jun. 2023.
- [23] National and Technical University of Athens, "Aerodynamic Coefficient | OpenWindLab," 2023. [Online]. Available: <https://openwindlab.net/#/graphs/aerodynamic-coefficient/2>
- [24] *EN 61400-12-1:2006, Wind turbines. Part 12-1 Power performance measurements of electricity producing wind turbines*. London: British Standards Institution, 2006.

APPENDIX

Parameter	Value	Unit	Parameter	Value	Unit
P_{nom}	700	W	I_{max}	20	A
V_{dc}	50	V	R_s	0.42	Ω
p	8	-	ϕ_f	0.11	Wb
L_s	1	mH	b	0.008	N.m.s/rad
J	0.66	kg.m ²	ρ_{air}	1.204	kg/m ³
$C_{p(max)}$	0.33		R_r	1.2	m
λ_{opt}	5.75		l_1	30	
K_{opt}	0.0088		l_3	10	
l_2	100				

TABLE II

SUMMARY OF THE EXPERIMENTAL SETUP SYSTEM PARAMETERS.

Proof of Theorem 1

The system described by (26) which state vector is $x = [e_d, e_q, e_{i_d}, e_{i_q}, e_\omega]^T \in \mathbb{R}^5$ has a unique equilibrium

$$x^* = [0, 0, 0, 0, 0]^T. \quad (54)$$

A Lyapunov function candidate is proposed such as

$$\begin{cases} V &= \beta(V_d + V_q) + V_\omega \\ V_d &= \frac{1}{2}Le_d^2 + \frac{1}{2}k_i e_{id}^2 \\ V_q &= \frac{1}{2}Le_q^2 + \frac{1}{2}k_i e_{iq}^2 \\ V_\omega &= \frac{1}{2}e_\omega^2 \end{cases}$$

with $\beta > 0$ and $k_i > 0$. The derivative in the d axis is given by

$$\begin{aligned} \dot{V}_d &= Le_d \dot{e}_d + k_i e_{id} \dot{e}_{id} \\ &= -(k_p + R)e_d^2 + pL(e_\omega + \omega^*)e_q e_d + pLe_\omega e_d i_q^\# \end{aligned} \quad (55)$$

and in the q axis by

$$\begin{aligned} \dot{V}_q &= Le_q \dot{e}_q + k_i e_{iq} \dot{e}_{iq} \\ &= -(k_p + R)e_q^2 - pL(e_\omega + \omega^*)e_d e_q \\ &\quad - p(\phi_f + Li_d^\#)e_\omega e_q. \end{aligned} \quad (56)$$

Hence,

$$\begin{aligned} \dot{V}_d + \dot{V}_q &= -(k_p + R)e_d^2 - (k_p + R)e_q^2 + pLe_\omega e_d i_q^\# \\ &\quad - p(\phi_f + Li_d^\#)e_\omega e_q. \end{aligned} \quad (57)$$

Moreover, the derivative for V_ω can be given by

$$\begin{aligned} \dot{V}_\omega &= e_\omega \dot{e}_\omega \\ &= \frac{\frac{3}{2}p\phi_f}{J}e_\omega e_q + \frac{\frac{3}{2}p\phi_f}{J}e_\omega i_q^\# - \frac{b}{J}e_\omega^2 - \frac{b}{J}e_\omega \omega^*. \end{aligned} \quad (58)$$

Since $\omega^* = \frac{3}{2b}p\phi_f i_q^\#$, eq. (58) can be simplified such as

$$\dot{V}_\omega = \frac{\frac{3}{2}p\phi_f}{J}e_\omega e_q - \frac{b}{J}e_\omega^2. \quad (59)$$

From eqs. (55), (56), (59), the Lyapunov function derivative can be written as

$$\begin{aligned} \dot{V} &= -(k_p + R)\beta e_d^2 - (k_p + R)\beta e_q^2 - \frac{b}{J}e_\omega^2 + pL\beta e_\omega e_d i_q^\# \\ &\quad - p\beta(\phi_f + Li_d^\#)e_\omega e_q + \frac{\frac{3}{2}p\phi_f}{J}e_\omega e_q \end{aligned} \quad (60)$$

which can be re-written as

$$\dot{V} = [e_d \quad e_q \quad e_\omega] \underbrace{\begin{bmatrix} -a\beta & 0 & \beta d \\ 0 & -a\beta & e - \beta c \\ \beta d & e - \beta c & -\frac{b}{J} \end{bmatrix}}_M \begin{bmatrix} e_d \\ e_q \\ e_\omega \end{bmatrix} \quad (61)$$

with $a = k_p + R$, $c = p(\phi_f + Li_d^\#)/2$, $d = \frac{1}{2}pLi_q^\#$ and $e = \frac{\frac{3}{2}p\phi_f}{2J}$. The determinant is given by

$$\det M = \frac{-\gamma + a\beta}{J} (J\gamma^2 + (b + Ja\beta)\gamma - J(e^2 + \beta^2 c^2 + \beta^2 d^2) + 2Jce\beta + ab\beta). \quad (62)$$

implying three eigenvalues $\gamma_1, \gamma_2, \gamma_3$. The first eigenvalue is written as

$$\gamma_1 = -a\beta. \quad (63)$$

Since $\beta > 0$, the following condition must be met to ensure that the first eigenvalue is negative

$$k_p > -R. \quad (64)$$

Given this condition, the coefficients factors of γ and γ^2 are positive, since J and b are positive parameters. Thus, γ_2, γ_3 are negative if

$$P(\beta) = -J(e^2 + \beta^2 c^2 + \beta^2 d^2) + 2Jce\beta + ab\beta > 0. \quad (65)$$

Since $P(\beta)$ is a downwards parabola, it can be positive if $\max P(\beta) > 0$. One can write

$$\frac{dP}{d\beta} = -2J(c^2 + d^2)\beta + 2Jce + ab \quad (66)$$

hence, $\beta_{max} = \frac{2Jce+ab}{2J(c^2+d^2)}$ and

$$P(\beta_{max}) = \frac{1}{4J(c^2 + d^2)}Q(a) \quad (67)$$

with $Q(a) = -4J^2 d^2 e^2 + 4cJabe + a^2 b^2$ which is an upwards parabola with two roots $\{a_1, a_2\} \in \mathbb{R}^2$ with $a_2 > 0 > a_1$ and

$$a_2 = \frac{2(Je\sqrt{c^2 + d^2} - Jce)}{b}. \quad (68)$$

Inserting the expressions of c, d, e in eq. (68) leads to

$$a_2 = \frac{3}{4b}p\phi_f \sqrt{p^2(\phi_f + Li_d^\#)^2 + (Li_q^\# p)^2} - \frac{3p^2\phi_f(\phi_f + Li_d^\#)}{4b}. \quad (69)$$

Hence, one can write that

$$a > a_2 \Rightarrow Q(a) > 0 \Rightarrow P(\beta_{max}) > 0 \Rightarrow \{\gamma_2, \gamma_3\} < 0 \quad (70)$$

In a nutshell, the following conditions

$$\begin{cases} k_p > -R \\ k_p > a_2 - R \end{cases} \quad (71)$$

shall be met to guarantee that $\dot{V} < 0$. Since R is a positive physical parameter and $a_2 > 0$ the dominant condition is

$$k_p > a_2 - R. \quad (72)$$

If the condition (72) is satisfied, $\dot{V} \leq 0 \quad \forall x \in \mathbb{R}^5$ which proves that the equilibrium $x^* = 0$ is globally stable. Let S be the set of solutions where $\dot{V} = 0$, i.e., $S = \{x \in \mathbb{R}^5 \mid e_d = e_q = e_\omega = 0\}$. The unique invariant solution of S is $x^* = 0$ thus, according to LaSalle's theorem, it can be concluded that the convergence is asymptotic to the equilibrium point. Finally, since $V > 0$ for all $x \neq 0$ and $V(0) = 0$ it results that the system is GAS, which ends the proof.

Proof of Eq. (34)

From Eq. (32), a slightly more restrictive condition is given by

$$l_1 > \frac{L_o}{L} \cdot \max(|e_\alpha|, |e_\beta|) + \max(|\pi_\alpha|, |\pi_\beta|). \quad (73)$$

Let us find a bound for the perturbation terms Π_α and Π_β

$$\begin{aligned} |\Pi_\alpha| &= \left| \left(\frac{R\delta_L}{L} - \delta_R \right) i_\alpha - \frac{\delta_L}{L} v_\alpha \right|, \\ &\leq \left(\frac{R|\delta_L|}{L} + |\delta_R| \right) I_{max} + \frac{|\delta_L|}{L} V_{max}, \\ &\leq \left(R_{max} \frac{\Delta_L}{L_{min}} - \Delta_R \right) I_{max} + \frac{\Delta_L}{L_{min}} V_{max} = \Pi_{max} \end{aligned} \quad (74)$$

Applying the same reasoning for Π_β gives rise to the same bound Π_{max} , which leads to $\Pi_{max} \geq \max(|\pi_\alpha|, |\pi_\beta|)$. Since

$$\frac{L_o}{L} e_{\alpha\beta} \leq \frac{L_o}{L_{min}} E_{max}, \quad (75)$$

the bound on l_1 naturally comes as

$$l_1 > \frac{L_o}{L_{min}} E_{max} + \Pi_{max}, \quad (76)$$

which proves the bound given by Eq. (34).

Proof of Eq. (39): Using the inverse of Eq. (10) in Eq. (37) gives

$$\begin{aligned} \hat{e}_\alpha &= -\frac{L_o}{L} p\phi_f \omega \sin(\theta_e) + \frac{R\delta_L - \delta_R L}{L} (i_d \cos(\theta_e) - i_q \sin(\theta_e)) \\ &\quad - \frac{\delta_L}{L} (v_d \cos(\theta_e) - v_q \sin(\theta_e)), \\ \hat{e}_\beta &= \frac{L_o}{L} p\phi_f \omega \cos(\theta_e) + \frac{R\delta_L - \delta_R L}{L} (i_d \sin(\theta_e) + i_q \cos(\theta_e)) \\ &\quad - \frac{\delta_L}{L} (v_d \sin(\theta_e) + v_q \cos(\theta_e)). \end{aligned} \quad (77)$$



Adrien Prévost received the M.S. degree in electrical engineering from Institut National des Sciences Appliquées de Lyon (INSA Lyon), Villeurbanne, France, in 2020. He received the Ph.D. degree in control theory from INSA Lyon in 2024. He is currently a post-doc researcher at G2ELab, Institut National Polytechnique (INP) Grenoble, France. His research includes modeling, design, control and technico-environmental optimization of electrical machine-converter systems.



Vincent Léchappé received the M.S. and Ph.D. degrees in control theory from the Ecole Centrale de Nantes, Nantes, France, in 2012 and 2015, respectively, both in control theory. He was a Lecturer with the School of Engineering and Physics, the University of the South Pacific, Suva, Fiji, in 2016. He joined Griffith University in Australia for a Postdoctoral stay, in 2017. In November 2017, he joined INSA Lyon, France, where he is currently an Associate Professor at Electrical Engineering Department. His research interests include control

and observation of electrical machines and their environmental impacts.

After manipulations, it leads to

$$\begin{aligned} \hat{e}_\alpha &= -x \sin(\theta_e) + y \cos(\theta_e), \\ \hat{e}_\beta &= x \cos(\theta_e) + y \sin(\theta_e) \end{aligned} \quad (78)$$

with

$$\begin{aligned} x &= \frac{L_o}{L} p\phi_f \omega - \frac{\delta_L}{L} v_q + \frac{R\delta_L - \delta_R L}{L} i_q, \\ y &= -\frac{\delta_L}{L} v_d + \frac{R\delta_L - \delta_R L}{L} i_d. \end{aligned} \quad (79)$$

Injecting Eq. (38) in Eq. (79) allows simplifying the terms a and b gives:

$$\begin{aligned} x &= \frac{L+\delta_L}{L} p\phi_f \omega - \frac{\delta_L}{L} (Ri_q^* + p\omega Li_d^* + p\phi_f \omega) \\ &\quad + \frac{R\delta_L}{L} i_q^* - \frac{\delta_R L}{L} i_q^*, \\ &= p\omega (\phi_f - i_d^* \delta_L) - \delta_R i_q^*, \\ y &= -\frac{\delta_L}{L} (Ri_d^* - p\omega Li_q^*) + \frac{R\delta_L}{L} i_d^* - \frac{\delta_R L}{L} i_d^*, \\ &= -i_d^* \delta_R + i_q^* p\omega \delta_L \end{aligned} \quad (80)$$

which ends the proof.



Romain Delpoux received the M.S. degree in control system and mechatronics from the Chalmers University of Technology, Gothenburg, Sweden, in 2009 and the Ph.D. degree in control theory, data and signal processing from the École Centrale de Lille, Villeneuve-d'Ascq, France, in 2012. In September 2014, he joined INSA Lyon, Villeurbanne, France, and the Ampere Laboratory, where he is currently an Associate Professor. His research interests include embedded control applications for power electronics systems.



Xavier Brun was born in France in 1973. He received the Ph.D. degree from the Institut National des Sciences Appliquées de Lyon (INSA Lyon), Villeurbanne, France, in 1999. He became an Associate Professor with the Laboratoire d'Automatique Industrielle, INSA Lyon, in 2001. Since 2011, he has been a Professor at the Laboratoire Ampere, INSA Lyon, France. His current research interests include control for mechatronic and fluid power systems.